Title

A study of changes in deep fractured rock permeability due to coupled hydro-mechanical effects

Authors

Figueiredo, Bruno
Tsang, Chin-Fu
Rutqvist, Jonny
et al.

Publication Date

2015-10-01

DOI

10.1016/j.ijrmms.2015.08.011

Peer reviewed

A study of changes in deep fractured rock permeability due to coupled hydro-mechanical effects

Bruno Figueiredo[a], Chin-Fu Tsang[a,b], Jonny Rutqvist[b], Auli Niemi[a]

[a] Uppsala University, Uppsala, Sweden
[b] Lawrence Berkeley National Laboratory, Berkeley, CA, United States

Available online 27 September 2015.
https://doi.org/10.1016/j.ijrmms.2015.08.011Get rights and content

Highlights

- Hydro-mechanical effects are studied for a realistic fractured rock domain.
- Stress distribution over 2D fracture network studied as a function of pore pressure.
- Failure or fracturing occurs not as fracture extensions but as failure of a region.
- A pore pressure increase changes pressure gradient distribution and flow paths.

Abstract

This paper presents a numerical study of the hydro-mechanical behaviour of a fractured rock domain at 1000 m depth below the land surface as a function of different levels of fluid pore pressure. A 2D fractured rock domain is adopted based on data obtained from outcrop mapping, displaying multiple fracture sets, fracture intersections, dead-end and curved fractures. A continuum based numerical model is used to evaluate the effects of compressive boundary stresses, cracking by tension failure in the intact rock and fractures and shear displacement along fractures on its equivalent permeability. Two *in situ* stress boundary conditions are considered: an isotropic case SR1 with the two horizontal boundary compressive stresses having the same magnitude, and an anisotropic case SR2 with the ratio between these compressive stress components set to be 2. In the SR2 case, changes in the local stress and stress ratio distributions due to different fluid pore pressure levels are anisotropic and more significant than in the SR1 case, because of tension failures in the intact rock forming bridges between fractures. These failure regions opened new flow connections between fractures and thereby caused important anisotropic changes in the flow paths, and significant decrease in local gradients of fluid pore pressure. The equivalent permeability increases sharply when the fluid pore pressure is approximately 90% of the magnitude of the minimum stress at the boundaries of the fractured rock domain. Results show that the equivalent permeability of the fractured rock domain is most sensitive to the fractures normal stiffness, the permeability of the tension failure regions and the power-law exponent for permeability change.

1. Introduction

Hydro-mechanical coupling in fractured rock masses is an important issue for many rock mechanics and hydrogeology applications,[1] particularly in the study of hydrogeology of deep formations at the depth of 1 km

or more.[2] Fractured rock masses are composed of intact rock materials and fractures, with the latter acting as the main pathways for fluid flow. The fractures usually consist of several fracture sets, fracture intersections, dead-end and curved fractures. Apertures of fractures can change due to rock mechanical effects, such as normal stress-induced compression or tension, and shear stress-induced dilation. Hence, the permeability of fractured rock masses and its anisotropy is stress dependent.[3]

The stresses at various locations over a fractured rock domain are naturally different from the far-field stresses, because of local stress concentrations induced by the existing fractures. There are several measurement techniques to determine *in situ* stresses in rock masses. Depending on the domain of application, the most commonly used stress determination techniques include hydraulic methods, relief methods and jacking methods. More techniques exist, and comprehensive reviews of stress determination methods may be found, for example, in Refs. 4 and 5. Although those techniques enable to determine the far-field stresses, the measurement results can be influenced by various factors, such as local heterogeneities, pre-existing fractures and spatial variability of the rock mass properties. Since the hydro-mechanical behaviour of fractures and the intact rock at any point of interest is dependent on the local stress changes, which in turn depends on the complexity of the near-field fracture pattern, there is a need to understand how these local changes are different from the far-field stresses.

Numerical studies of the coupled hydro-mechanical effects in fractured rock masses have been conducted using different methods, such as discrete and combined continuum–discrete based models.6, 7, 8, 9, 10, 11 Discrete based models, while more realistic for discontinuous media, have the limitation of not considering permeable intact rock and are time consuming for modelling hydro-mechanical behaviour of fractured rock domains with curved or dead-end fractures. Continuum based finite difference codes require a representation of discrete fracture behaviour with appropriate hydro-mechanical properties by an elemental cell, but they can have the advantage of being able to model fractures that are sealed and filled with mineral materials and are less time consuming. Furthermore, important phenomena such as changes in the permeability field and flow paths due to tension failure regions in the intact rock between fractures can be included. An important open issue is how much of the conclusions based on continuum based code are valid in understanding the mechanical and hydro-mechanical behaviour of a fractured rock domain which is a discontinuous medium. Continuum based models have been applied to simulate fractures propagation in fractured rocks.12, 13The stress intensity factors obtained with such modelling are in good agreement with the available analytical solutions. In Ref. 14, a numerical method for fragmentation is presented that combines the finite element method with the impulse-based discrete element method. Results for fracture growth within each three-dimensional fragment are in good agreement with experimental data. A comparison of the results obtained with a continuum and discrete fracture based models on fracture opening and sliding in response to fluid injection in a geothermal reservoir, was made in Ref. 15. The results obtained with the two models were found to be in agreement. In Ref. 16, a comparison between results obtained with a continuum-based model and discrete fracture and discontinuous models, was done. A good agreement was also found for the coupled hydro-mechanical fracture flow.

For our study of coupled hydro-mechanical effects within a fractured rock domain, as a function of different levels of fluid pore pressure, we use an actual observed fracture geometry with multiple fracture sets, fracture intersections, curved and dead-end fractures, obtained by outcrop mapping. The changes in fluid pore fluid pressure could be due to injection wells in the neighbourhood, e.g. during hydraulic stimulation of a reservoir, regional hydrogeological changes, or seismic events. The consideration of such a complex fractured rock domain enables us to study the coupled hydro-mechanical effects with focus on those issues related to the complexity of multiple fractures. Our goal is to draw general conclusions on these effects in complex fractured systems that do not depend on exact details of the complexity.

This paper presents a two-dimensional finite-difference model, developed in FLAC3D,[17] to study the coupled hydro-mechanical effects of the considered fractured rock domain. We study hydro-mechanical effects as a result of different levels of fluid pore pressure under constant external load, including the effects of tension in the intact rock and fractures and shear displacement in the fractures. The main objectives of the paper are to (1) analyse tension failure regions in the intact rock and fractures caused by different levels of fluid pore pressure, (2) evaluate the changes in the stress field induced by the occurrence of failure regions, (3) evaluate the changes in the fluid pore pressure field and flow paths, induced by changes in the stress field and (4) evaluate the changes in the equivalent permeability and permeability anisotropy.

A sensitivity analysis is made to study the influence of the tensile strength of the fractures, the fractures normal stiffness, the permeability of the tension failure regions and the power-law exponent of the relation used to calculate changes in permeability. The paper is completed with discussion and some concluding remarks.

2. Problem definition and selection of fracture rock pattern from outcrop maps

A fractured rock domain pattern for carbonate reservoir was obtained by using surface outcrop information.[18] Two sets of fractures are identified from outcrop mapping, with different orientations. The fracture sets 1 and 2 are sub-horizontal and sub-vertical, respectively. In our study, the original pattern was modified. Some fractures endings were extrapolated till the outcrop boundaries to ensure that flow occurs in two orthogonal directions, between two opposite boundaries. An area 1 m by 1 m (Fig. 1) is taken to carry out the stress-dependent permeability analysis as a function of fluid pore pressure. The plane of the fractured rock domain pattern is horizontal and the origin of the x and y-axis system is placed in the centre of the studied region.

Download high-res image (356KB)

Download full-size image

Fig. 1. Fractured rock domain pattern obtained by surface outcrop information. The inset shows the studied domain, with the fracture sets 1 and 2 (adapted from Ref. 18).

The presented fractured rock domain contains straight and curved fractures, fracture intersections, dead-end fractures and fracture tips adjacent to other fractures. Let us now assume that this outcrop is located at 1000 m depth with an equilibrium stress state resulting from the *in situ* stresses and the fluid pore pressure at this depth. This forms the basis for a numerical study of the hydro-mechanical behaviour of the fractured rock domain with different levels of fluid pore pressure.

3. Numerical approach

3.1. Finite-difference numerical model

A 2D finite-difference model was developed in FLAC3D[17] to study the hydro-mechanical behaviour of the fractured rock domain. The model is a square region with 1 m side. The mesh consists of 40000 square elements which 0.5 cm side (Fig. 2). The two sets of fractures have the same hydraulic and mechanical properties. Necessary model parameters are listed in Table 1. The model is executed in a plane strain analysis. For the intact rock, a Mohr–Coulomb model with tension cut-off was used, in which the mechanical properties (elastic modulus E_R, Poisson's ratio v_R, cohesion c_R, friction angle ϕ_R, tensile strength σ_{tR}) are characteristic of limestone rocks.[19], [20] The tensile strength σ_{tR} of the intact rock influences the fractures development, but similar results to those presented in this paper can also be obtained by changing the values of the different fluid pore pressure levels. The cohesion c_R influences the occurrence of shear failure in the intact rock. For a 30 MPa cohesion (see Table 1), shear failure does not occur in the intact rock and tension failure is the dominant mechanism. For small values of c_R, (e.g. 5 MPa) it was found that shear failure occurs in the intact rock and is more prevalent than tension failure, but the shear displacements and consequent changes in permeability are much smaller than those in the fractures. The other mechanical parameters were found not to influence significantly the results. Regarding the hydraulic properties, the values of 10^{-17} m^2 and 0.001 were assigned to the permeability k_R and porosity e_R of the intact rock, which are typical of limestone rocks.

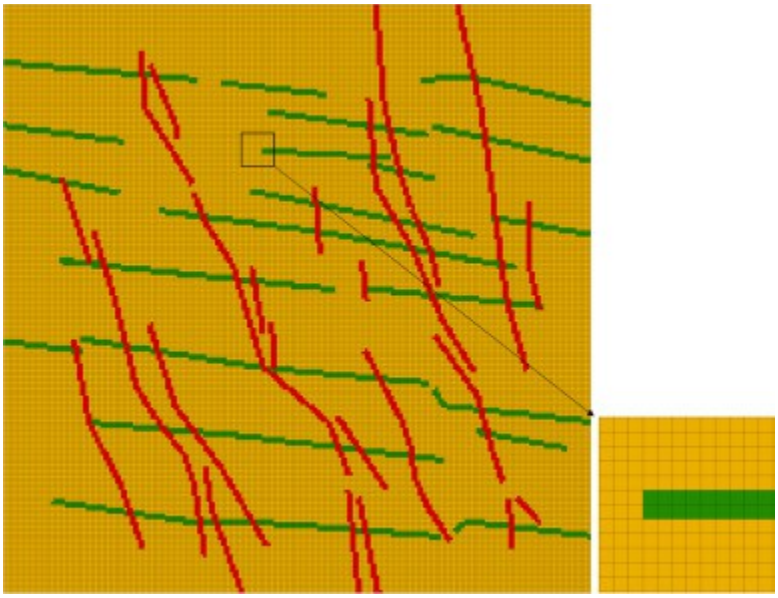

Download high-res image (1MB)

Download full-size image

Fig. 2. Mesh of the finite-difference model to study the hydro-mechanical behaviour of the fractured rock domain.

Table 1. FLAC3D model parameters.

Intact rock	Elastic modulus E_R (GPa)	20
	Poisson's ratio ν_R	0.3
	Tensile strength σ_{tR} (MPa)	5
	Cohesion c_R (MPa)	30
	Friction angle ϕ_R (°)	25
	Permeability k_R (m²)	1.0×10^{-17}
	Porosity e_R	0.001
Fractures	Elastic modulus E_F (GPa)	4.0
	Poisson's ratio ν_F	0.18
	Tensile strength σ_{tF} (MPa)	0
	Friction angle ϕ_F (°)	25
	Dilation angle ψ_F (°)	5
	Normal stiffness k_n (GPa/m)	1000
	Cohesion c_F (MPa)	0
	Aperture (μm)	30
	Permeability k_F (m²)	4.5×10^{-13}
	Porosity e_F	0.01

The shear stress-displacement fracture behaviour is modelled by a Mohr–Coulomb model with tension cut-off. The mechanical properties of the fractures (Poisson's ratio ν_F, friction angle ϕ_F, dilation angle ψ_F, cohesion c_F, fractures aperture b_h) were extracted from Ref. 3. The fracture normal stiffness k_n was assumed to be

1000 GPa/m. The tensile strength σ_{tF} for fractures was assumed to be zero. Further, a sensitivity analysis is done to study the influence of these two parameters on the obtained results (see 5.2 Effect of the tensile strength of the fractures, 5.3 Effect of the fractures normal stiffness).

According to,[16] fractures with filling material can be model as an equivalent solid material, in which the elastic modulus E_F of the elements intersected by a fracture trace is calculated according with the following equation:

$$\frac{1}{E_F} = \frac{1}{E_R} + \frac{1}{k_n d}, \quad (1)$$

where d is the element size (0.005 m).

To check if the used mesh enables to obtain a good estimate of the stresses close to the fractures, a very simple model with one vertical fracture and with a length 2c of 0.12 m, was developed (Fig. 3a). It was assumed that the fracture has no filling material or is completely open with no fracture surface contacts (no stiffness or stress transfer through surface contacts). The geometry of the model and the mesh elements size are the same of those used in model developed to study the hydro-mechanical behaviour of the fractured rock domain (see Fig. 2). An elastic model was considered with the elastic constants (elastic modulus E_R and Poisson's ratio v_R) presented in Table 1. A stress σxxb of 50 MPa was applied on the boundaries perpendicular to the x-axis (see Fig. 3a). The variation in the ratio between fracture normal stress σ_{xx} and boundary stress σxxb with distance $r/2c$ along the lines x=0 and y=0 away from the fracture was obtained and compared with the analytical solution presented in Ref. 21. Results of this comparison are shown in Fig. 3b. The figure shows that, close to the fracture, the difference between the solution provided by[21] and FLAC3D is smaller than 5%, which enables to conclude that the calculated stress redistribution and concentrations around fractures are accurately represented in our model. In our study, fractures with filling material or with stress transfer through surface contacts were considered. This is a more realistic scenario because it enables to consider changes in fractures aperture caused by changes in the effective stress normal to the fractures.

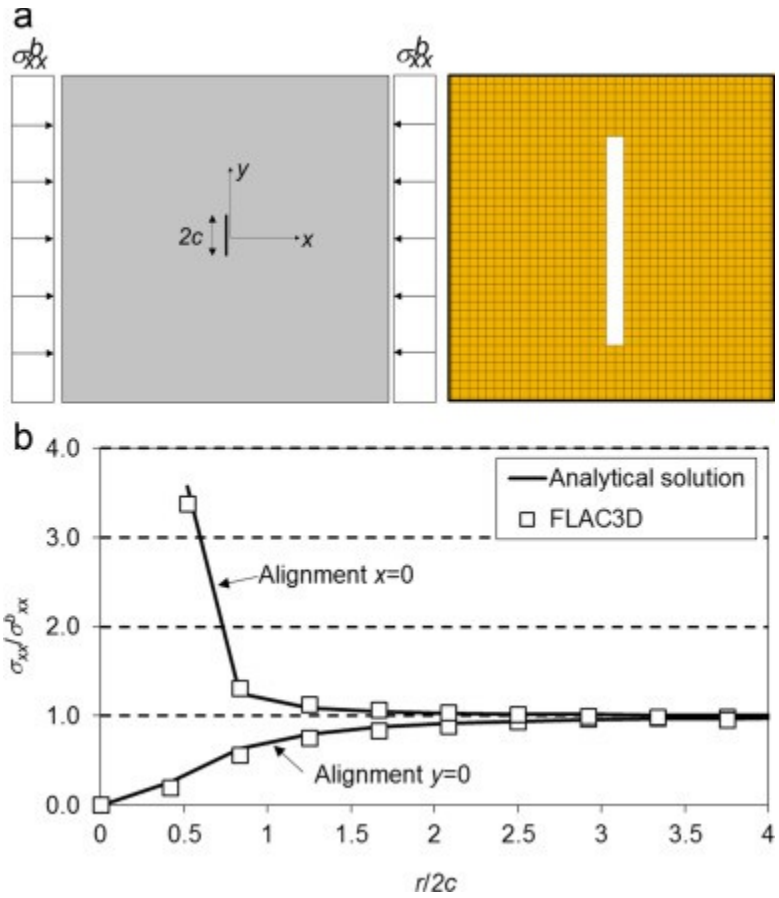

Download high-res image (404KB)
Download full-size image

Fig. 3. (a) Detail of the mesh to study the behaviour of a single fracture with length 2*c* (b) variation of the fracture normal stress as a function of the normalised distance *r/2c* away from the fracture, along the lines *x*=0 and *y*=0.

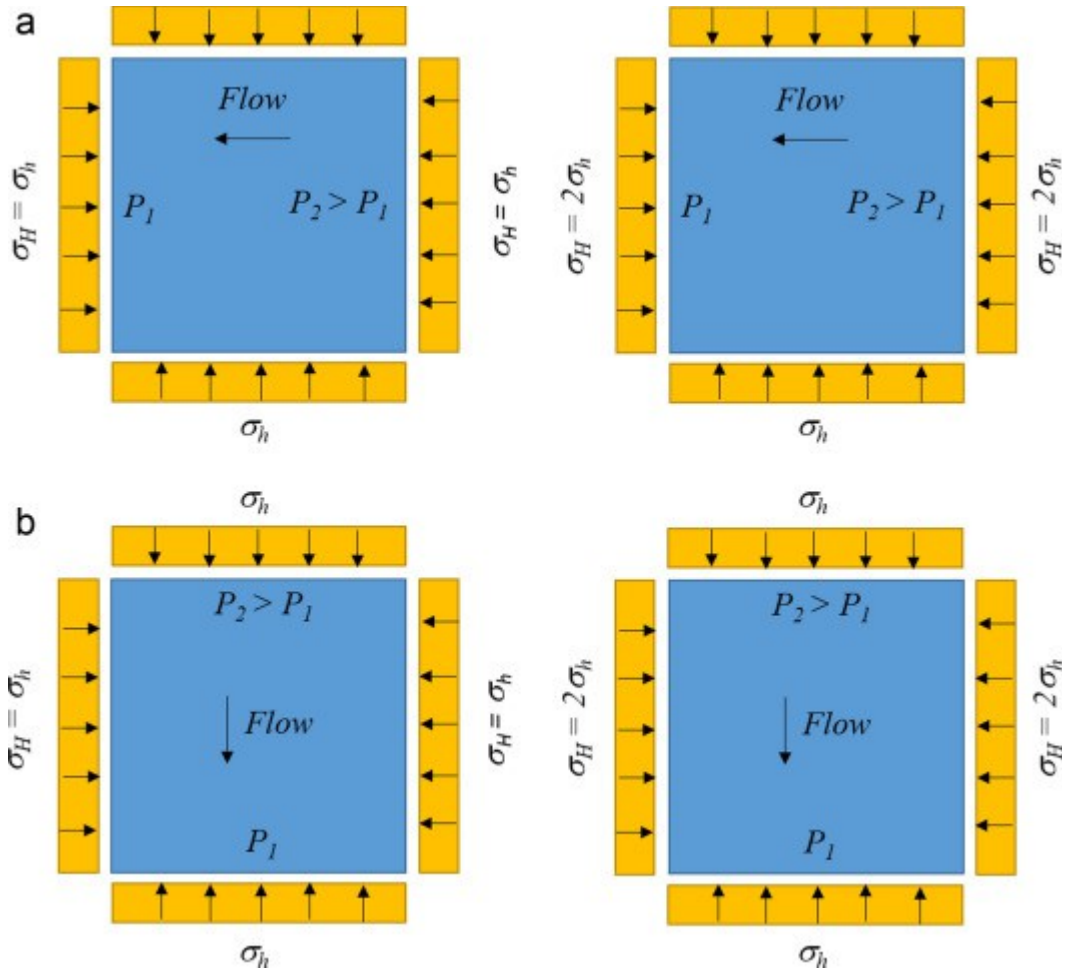

Download high-res image (397KB)

Download full-size image

Fig. 4. Boundary loading and fluid pore pressure conditions (a) flow along the *x*-direction (b) flow along the *y*-direction: σ_H and σ_h are the maximum and minimum boundary stresses, respectively, in the plane of the fracture pattern; P_1 and P_2 are the fluid pore pressure in two opposite boundaries.

The hydraulic behaviour of the fractures may be described in terms of the flow transmissivity and the normal and shear stiffness of the fractures. Laboratory experiments on single fractures show that the fracture transmissivity can be very sensitivity to changes in stress normal to the fractures as well as to shear displacement. Thus, mechanically induced changes in the fracture's ability to conduct fluid may be estimated using the cubic relations between flow along an open fracture and fractures aperture[1]:

$$T = \frac{b_h^3 \rho g}{12\mu}, \tag{2}$$

where T is the fracture transmissivity, b_h is fracture aperture, ρ and μ are fluid density and viscosity, respectively, and g is the acceleration of gravity.

The permeability k_F of the fracture is related to the fracture aperture b_h by the cubic law:

$$k_F = \frac{b_h^3}{12d}, \tag{3}$$

where d is element size (0.005 m).

Based on a fractures aperture of 30 μm (see Table 1), Eqs. (2), (3)lead to a fracture transmissivity T of 2.2×10^{-8} m^2/s and permeability of fractures k_F of 4.5×10^{-13} m^2, respectively. The porosity e_F of an element representing a fracture was assumed to have a value 10 times larger than the porosity of the intact rock, and in this way, is equal to 0.01. This is approximately equal to the equivalent fracture porosity ϕ within the fracture elements calculated by

$$\phi = \frac{b_h}{d}, \qquad (4)$$

where b_h the fracture aperture and d is the element size. Changes in permeability were found to be sensitivity to porosity of the fractures. Their magnitude becomes less significant as the porosity of the fractures increases. If the porosity was smaller than 0.01, changes in permeability would be more significant than those reported in this paper. However, the main conclusions extracted from this study, would be the same.

3.2. Loading conditions and fluid pore pressure

By assuming a vertical gradient of 0.027 MPa/m, the magnitude of the vertical stress component (σ_v) at 1000 m depth below the surface is 27 MPa. Two loading cases are considered: an isotropic case SR1, in which the maximum (σ_H) and minimum (σ_h) horizontal stresses have the same magnitude which is equal to the vertical stress magnitude (σ_v); and an anisotropic case SR2, in which the magnitude of the maximum horizontal stress (σ_H) is two times the magnitude of the minimum horizontal stress (σ_h), which is equal to the vertical stress magnitude (σ_v). The stresses are applied normal to the boundaries which are free to move. No shear stresses are considered at the boundaries (Fig. 4).

By assuming that the water table is located at the land surface and a fluid pore pressure vertical gradient of 0.01 MPa/m, at 1000 m depth below the surface the fluid pore pressure is 10 MPa. Let us also assume that there is a pressure gradient across the fractured rock under study with a magnitude of 0.25 MPa/m, which may result from pumping in a borehole located nearby the fractured rock domain. Thus, one of the lateral boundaries of the fractured rock domain has a fluid pore pressure of P_1 and the opposite boundary will be at a pressure P_2=P_1+0.25 MPa. Then flow occurs from the $P_2$to P_1 boundary. The fluid pore pressure gradient was considered in two separate cases in the x and y directions of the fractured rock domain (Fig. 4), with no flow in the opposite boundaries.

In our study, different levels of fluid pore pressure P_1 and P_2 were considered: 10, 15, 20 and 25 MPa, for P_1, and 10.25, 15.25, 20.25 and 25.25, for P_2, respectively. The fluid pore pressure P_1 was not considered to be more than 25 MPa, in order to limit the fluid pressure to below lithostatic (vertical) stress to avoid horizontal fracturing of the entire model domain and vertical instability. In the results and discussions presented in this paper, the fluid pore pressure p refers to the fluid pore pressure P_1.

3.3. Permeability changes in the fractures and tension failure regions

In fractured rock masses, effective stresses (which include effect of fluid pore pressure) induce changes in hydraulic properties, such as the permeability and porosity. In the natural fractures the initial values of the porosity and permeability were corrected by taking into account changes in volumetric strains,[22] which are

defined as the ratio of the change in volume of the fracture elements to its original volume. A model developed and applied by Ref. 23 to consider permeability changes in petroleum reservoirs was used. This model relates first the porosity ϕ at a given stress to the isotropic volumetric strain variation ε_v in the fracture elements and then the permeability k at a given stress to changes in porosity, according to the following equations:

$$\phi = 1 - (1 - \phi_i)\exp(-\varepsilon_v), \tag{5}$$

$$k = k_i \left(\frac{\phi}{\phi_i}\right)^n, \tag{6}$$

where ϕ_i is the initial porosity, k_i is the initial permeability and n is a power law exponent.

Changes in volumetric strains result from changes in the fractures normal stress. In this way, changes in fractures aperture are considered: if the compressive stress normal to the fractures increases, the fractures aperture decreases and the compressive volumetric strains increase. Volumetric strains include elastic and plastic components. Elastic component is originated by elastic shear deformation until the Mohr–Coulomb criterion is reached. After this criterion is reached, shear failure occurs and variations in the volumetric strains are also caused by plastic shear deformation and associated shear dilation. Shear dilation leads to an increase in the fractures aperture and a subsequent increase in the initial values of porosity and permeability of the fractures.

The empirical relation between permeability and porosity expressed in Eq. (6) has been shown to be widely applicable to geological materials. Even though if the exponent n could vary between 3 and 25 for consolidated geological materials,[24] we have set the exponent to 3, based on a cubic variation of the permeability with the aperture and porosity of the fracture elements[25]:

$$\frac{k}{k_i} = \left(\frac{b_h}{b_{hi}}\right)^3 = \left(\frac{\phi \cdot d}{\phi_i \cdot d}\right)^3 = \left(\frac{\phi}{\phi_i}\right)^3, \tag{7}$$

where b_{hi} is the initial aperture of the fractures. Further, a sensitivity analysis is done to study the influence of the value of the exponent n on the obtained results (see Section 5.5).

The tension failure regions in the intact rock that may connect the existing fractures, are considered to be similar to natural fractures; i.e., they are assumed to have the same initial porosity and permeability. In this way, extension of fractures has been modelled. Then, these initial values were corrected, according to Eqs. (5), (6), to take into account the stress-dependent behaviour. Further, a sensitivity analysis is done to study the influence of the initial value for the permeability of the tension failure regions on the obtained results (see Section 5.4).

3.4. Coupled hydro-mechanical calculation

The stress dependent-permeability of the fractured rock domain is governed by (1) local stress concentrations (2) the extent of dilation when the fractures undergo plastic deformation and (3) tension failure regions. In this section, the procedure for coupled hydro-mechanical analysis, is described.

A mechanical analysis was first carried out by considering the loading conditions SR1 and SR2 and the gradient with different fluid pore pressure P_1 and P_2 values (see Section 3.2) to calculate the stress field over the fractured rock domain. Fluid pore pressure leads to a decrease in the effective stresses over the fractured rock domain. In the regions where the tensile stresses exceed the tensile strength of the intact rock, tension failure occurs and the initial values of porosity and permeability of those regions are set to the respective values considered for natural fractures, as described in Section 3.3. In the natural fractures and tension failure regions, changes in porosity and permeability were considered as a function of changes in the volumetric strains, as described in Section 3.3.

By considering those changes in porosity and permeability, a hydraulic analysis was done to calculate the new fluid pore pressure distribution over the fractured rock domain. Then, a new mechanical analysis was done to calculate changes in the stress field induced by changes in the fluid pore pressure field. This procedure was repeated until the differences in fluid pore pressure and principal stresses obtained over the fractured rock domain, in two consecutive iterations, is negligible.

3.5. Calculation of flow characteristics and equivalent permeability

The flow rates along the *x* and *y*-directions, Q_x and Q_y, across the boundaries of the fractured rock can be calculated by using the following equations:

$$Q_x = A\frac{k_x}{\mu}\frac{\partial P}{\partial x}, \tag{8}$$

$$Q_y = A\frac{k_y}{\mu}\frac{\partial P}{\partial y}, \tag{9}$$

where *A* is the cross sectional area, k_x and k_y are the equivalent permeability's in the *x* and *y*-directions, respectively; μ is the dynamic viscosity, and $\partial P/\partial x$ and $\partial P/\partial y$ are the fluid pore pressure gradients across the boundaries in *x* and *y*-directions. Here, the equivalent permeability is a constant permeability to represent a heterogeneous medium. This is different from the notation of effective permeability, which is used for a medium that is statistically homogeneous on the large scale.[26]

The out-flow rates in the left or lower boundary of the fractured rock domain were calculated numerically with the FLAC3D code. Eqs. (8), (9) were used to back-calculate the values of k_x and k_y, respectively. The flow at the boundaries of the domain are identical for the heterogeneous medium and the equivalent homogeneous one, subjected to the same head gradient.

4. Results

In this section, we present the results of coupled hydro-mechanical analysis of the 2D fractured rock domain under different levels of fluid pore pressure. First, we consider the boundary loading conditions SR1 and SR2 and we analyse the tension failure regions in the intact rock as a function of different levels of fluid pore

pressure and study how these regions change the stress field over the fractured rock domain. Changes in volumetric strains in the fractures and tension failure regions, are also evaluated. Then, changes in the fluid pore pressure field and flow paths are analysed. Finally, changes in equivalent permeability and flow anisotropy as a function of different levels of fluid pore pressure are presented and discussed.

4.1. Results of tension failure regions and changes in volumetric strains

To quantify the tension failure regions, the percentage of the area of the fractured rock domain where tension failure in the intact rock occurs was calculated and shown in Fig. 5. Since the results are sensitivity mainly to the average fluid pore pressure and not to the pressure gradient, they are quite similar when the flow is along the *x*and *y*-directions. Thus, only the results obtained when the flow is along the *x*-direction are presented in this figure.

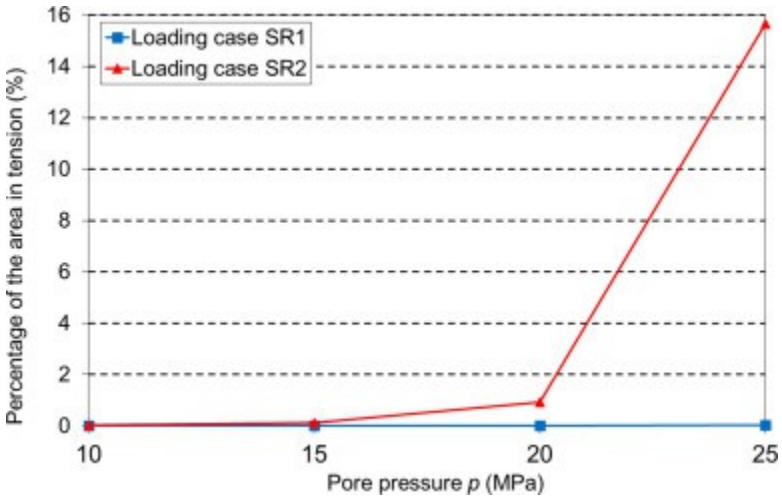

Download high-res image (181KB)

Download full-size image

Fig. 5. Percentage of the area of the fractured rock domain where tension failure in the intact rock occurs at different fluid pore pressure *p* levels.

The results in Fig. 5 indicate that almost no tensile failure occurs in loading case SR1. For all fluid pore pressure levels, the percentage of the fracture's domain area where the tensile strength of the intact rock is exceeded is smaller than 0.05%. In loading case SR2, the area of the tension failure ranges between approximately 0.03 and 16% of the area of the fractured rock domain, when the fluid pore pressure varies between 10 and 25 MPa, respectively.

Fig. 6 shows the tension failure regions and how they connect the existing fractures, when the fluid pore pressure *p* is 10, 15, 20 and 25 MPa. In this figure, the tension failure regions in the intact rock are represented by the black colour. The locations of the fracture connections are shown by the circles. The results displayed in this figure were obtained for the loading case SR2 and flow along the *x*-direction. Changes in flow rate at reference points 1 to 5, located on the left boundary of the FLAC3D model, will be analysed in Section 4.3. The figure shows an increase of the tension regions for a fluid pore pressure of 25 MPa, as suggested by the analysis of Fig. 5. This is because this fluid pore pressure value is very close to the magnitude of the minimum

boundary stress (27 MPa). In addition, for this fluid pore pressure level tension failure regions are found to be not localised single fracture extensions (as for a 20 MPa fluid pore pressure case), but regions of irregular shapes. The shape of a failure region depends on the magnitude of the local minimum principal stress, the tensile strength of the intact rock, the fluid pore pressure, and the geometry of the fracture system. The shape of the fracture regions obtained in this work is in good agreement with that obtained by Ref. 27 with several numerical methods, including boundary element, finite element, finite difference, particle mechanics, and elasto-plastic cellular automata methods.

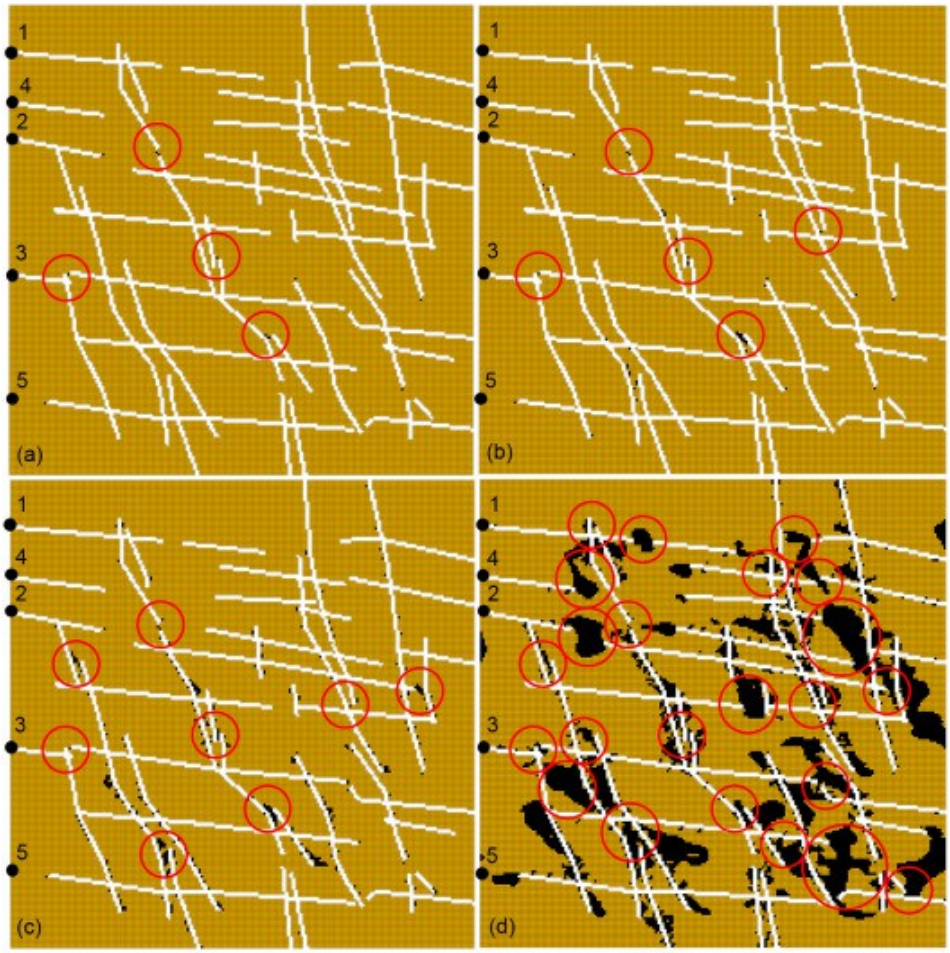

Download high-res image (3MB)

Download full-size image

Fig. 6. Tension failure regions in the intact rock for a fluid pore pressure *p* of (a) 10 MPa (b) 15 MPa (c) 20 MPa (d) 25 MPa, represented by the black colour (results obtained for the loading case SR2).

The FLAC3D code was used to calculate the mean values for the volumetric strains in the fracture sets (1 and 2) and the tension failure regions for different fluid pore pressure values. The mean values for the volumetric strains of the fractures and tension failure regions were also calculated. Fig. 7 shows the variation of the mean volumetric strains as a function of fluid pore pressure. The results obtained by considering the flow along the *x* and *y*-directions are similar, and hence, only the results obtained when the flow is along the *x*-direction are presented. They do not include the strain accumulated during the initial loading of the fractured rock domain. In this figure, the negative sign indicates the presence of tensile strains. Fig. 7 shows that for the

loading case SR1, when the fluid pore pressure varies between 10 and 25 MPa, the elements of the fracture set 1 get more compressed. In fracture set 2, the compression increases for a fluid pore pressure ranging between 10 and 20 MPa, and decreases when the fluid pore pressure is 25 MPa. For this fluid pore pressure level, tension strains are observed in the tension failure regions. This analysis shows that the volumetric strains in the fractures can be more compressive as a result of an increase in fluid pore pressure. This appears contrary to expectation, since it is expected that when the fluid pore pressure increases, the fractures aperture increases as a result of effective stress decreases. It was found that until a pore pressure of 25 MPa is applied, shear failure is the dominant mechanism over tension failure in the fractures. However, the shear dilation is not significant and the fractures aperture decreases for higher levels of fluid pore pressure, as a result of the expansion of the rock matrix that swells into the softer fractures. This will be more discussed in Section 5.1.

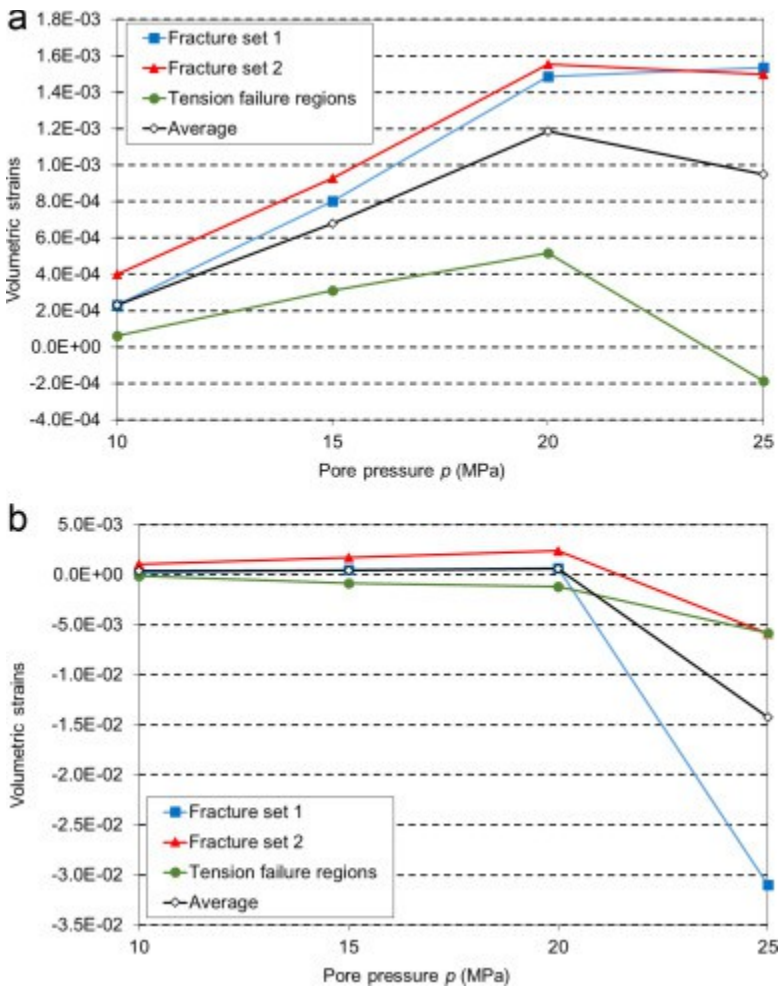

Download high-res image (452KB)

Download full-size image

Fig. 7. Mean volumetric strains obtained in the fracture sets and tension failure regions, for different fluid pore pressure p levels, for the (a) loading case SR1 and (b) loading case SR2.

For the loading case SR2, as it is observed in loading case SR1, the compressive strains in the fractures increase until a fluid pore pressure of 25 MPa is applied, because shear dilation is not enough to compensate for the compression induced by the intact rock into the softer fractures. The elements of the tension failure regions are in tension which increases for higher levels of fluid pore pressure. For a fluid pore pressure equal to

25 MPa, the tension failure in the intact rock and fractures increases significantly (see Fig. 5), which relieves some of the compressive volumetric strains and hence the mean fracture aperture increases. This analysis concludes that tension failure regions and changes in volumetric changes are more significant in loading case SR2.

4.2. Stress heterogeneity

This section aims to evaluate the stress heterogeneity over the fractured rock domain induced by different levels of fluid pore pressure. A comparison between the local stresses over the fractured rock domain and the boundary stresses, for both loading conditions SR1 and SR2, was made. Local stresses are the stresses that would be measured at a given point in the fractured rock mass.

Fig. 8, Fig. 9 show, for the loading cases SR1 and SR2, respectively, the contours of the maximum compressive principal stress (σ_I), minimum compressive principal stress (σ_{II}) and the ratio between the local maximum (σ_I) and minimum (σ_{II}) compressive principal stresses. These results were obtained by considering the flow along the *x*-direction and a fluid pore pressure *p* of 10 and 25 MPa.

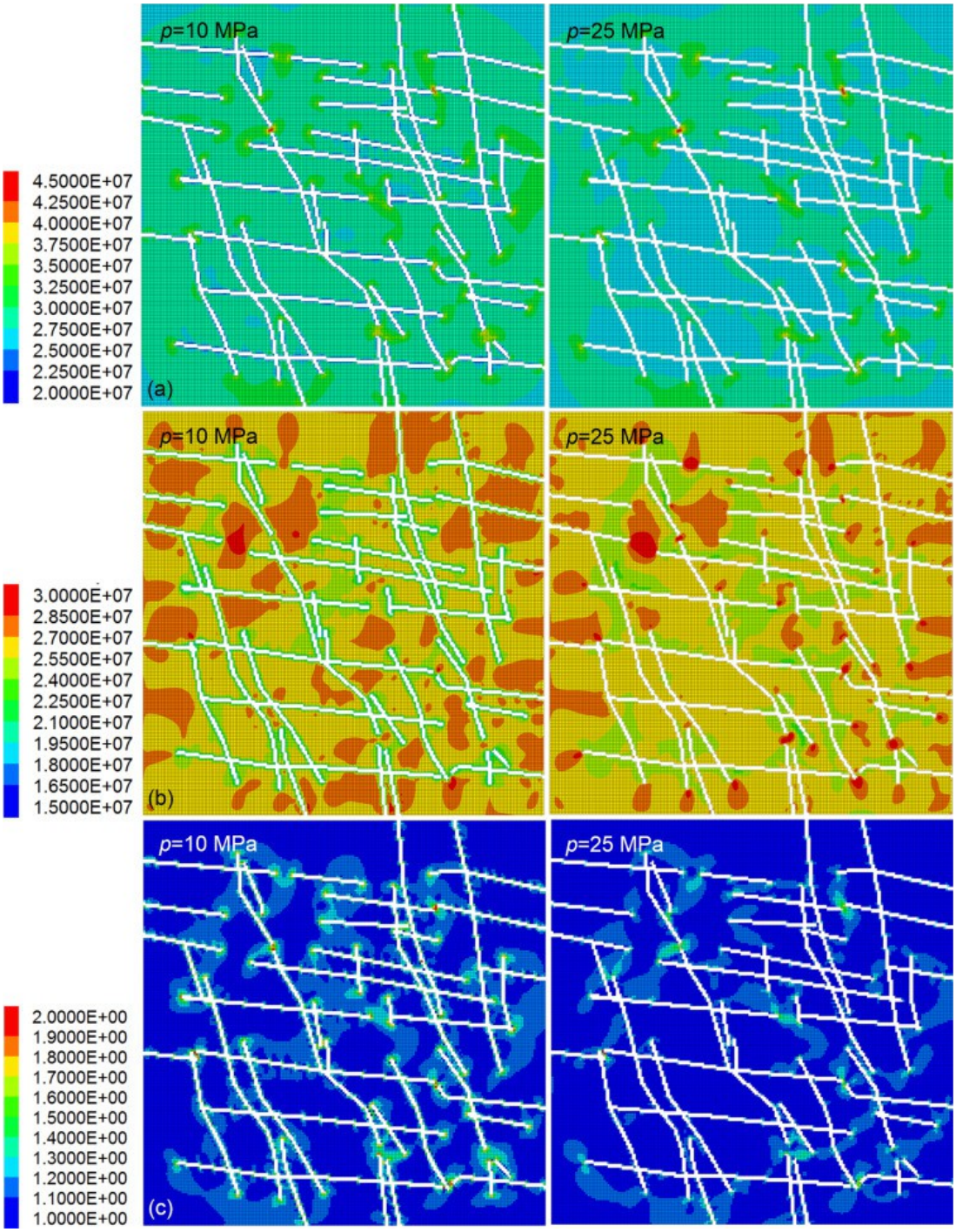

Download high-res image (7MB)

Download full-size image

Fig. 8. Contours of the (a) maximum compressive principal stress (σ_I) [Pa] (b) minimum compressive principal stress (σ_{II}) [Pa] and (c) ratio between the maximum (σ_I) and minimum (σ_{II}) compressive principal stresses for a fluid pore pressure p of 10 MPa (left column) and 25 MPa (right column) (results obtained for the loading case SR1).

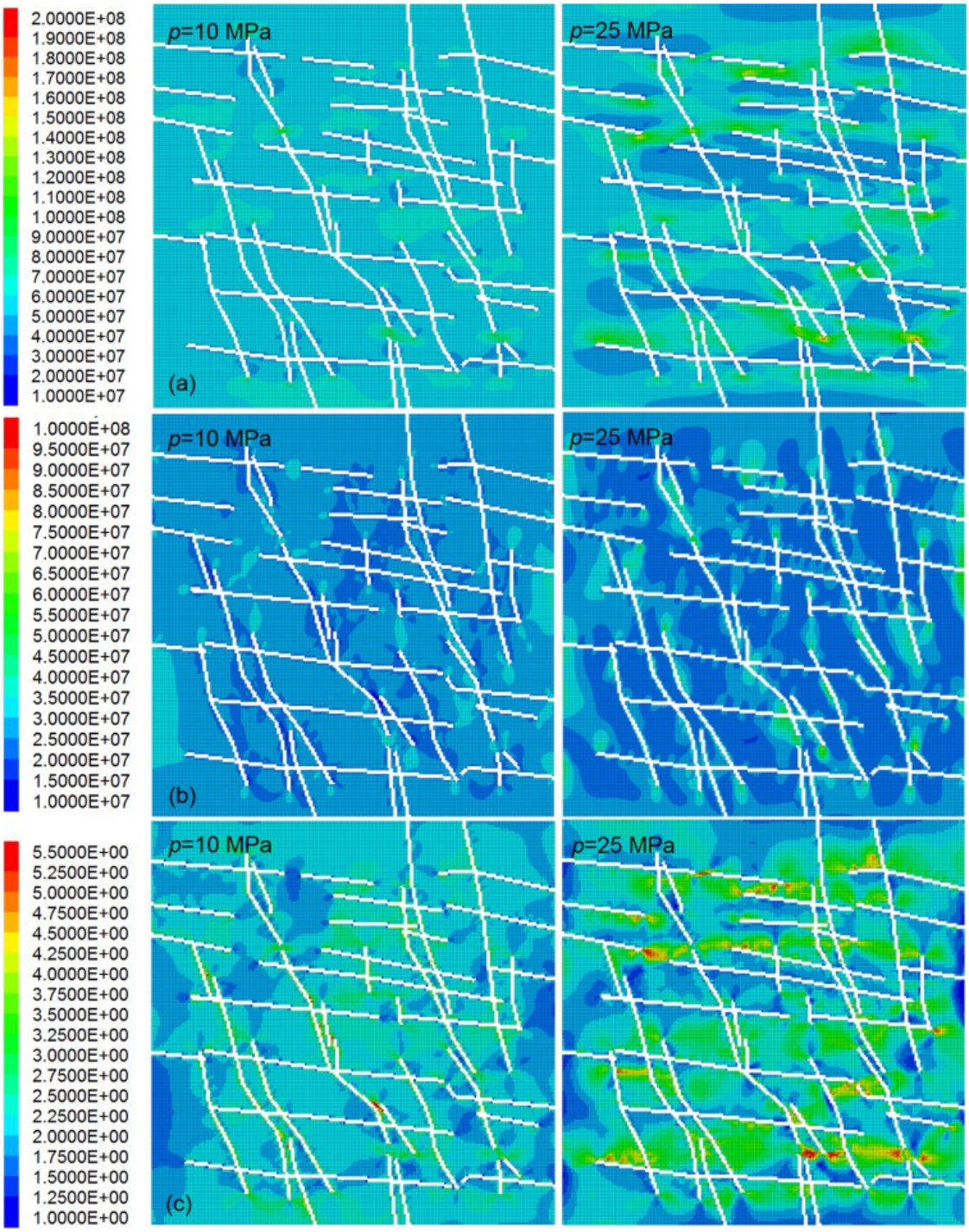

Download high-res image (7MB)

Download full-size image

Fig. 9. Contours of the (a) maximum compressive principal stress (σ_I) [Pa] (b) minimum compressive principal stress (σ_{II}) [Pa] and (c) ratio between the maximum (σ_I) and minimum (σ_{II}) compressive principal stresses for a fluid pore pressure p of 10 MPa (left column) and 25 MPa (right column) (results obtained for the loading case SR2).

The results show that, in loading case SR1, for a 25 MPa fluid pore pressure the magnitude of the maximum and minimum compressive principal stresses over the fractured rock domain is slightly smaller than the magnitude of those stress components obtained with a fluid pore pressure of 10 MPa. When a 25 MPa fluid pore pressure is applied, the local minimum compressive principal stress magnitude in the intact rock between

fractures can be about 75% of the minimum boundary stress magnitude. The ratio between the local maximum and minimum compressive principal stresses, obtained over the fractured rock domain with fluid pore pressures of 10 and 25 MPa, is similar and ranges between 1 and 2. Maximum values are located at vicinity of fracture endings and in the intact rock between nearby fractures.

In loading case SR2, the tension regions induce considerable differences in the total stresses obtained with fluid pore pressures of 10 and 25 MPa. In a significant part of the fractured rock domain, the magnitude of the local maximum and minimum compressive principal stresses obtained for a 25 MPa fluid pore pressure is smaller than the magnitude of those stress components obtained with a fluid pore pressure of 10 MPa. However, at some fractures tips and between some two adjacent existing fractures, the local principal stresses magnitude calculated with a fluid pore pressure of 25 MPa is greater than that obtained with a 10 MPa fluid pore pressure. The minimum value for the minimum principal stress in the intact rock between fractures is approximately 55% of the minimum boundary stress magnitude, which means that in some areas the tension failure can be initiated at fluid pressure much less than the boundary minimum principal stress. For a fluid pore pressure of 10 and 25 MPa, the stress ratio obtained over the fractured rock domain ranges approximately between 1.5 and 5.5. The ratio of 5.5, which is more than two times the correspondent boundary stress ratio of the fractured rock domain, is verified at location of some fracture endings and between two nearby fractures. When a 25 MPa fluid pore pressure is applied, the stress ratio over the fractured rock domain generally increases, in particular, at location of fracture endings and between two nearby fractures. The analysis of Fig. 5, Fig. 9 enables to conclude that generally failure regions are associated to a larger stress ratio that results from an increase in the magnitude of the local maximum compressive principal stress and a decrease in the local minimum compressive principal stress magnitude at those regions.

These results show that the local maximum compressive principal stress magnitude obtained over the fractured rock domain can be considerably larger than the boundary stress magnitudes. This can be understood from the softer mechanical properties of the fractures, so that the stress loads from the boundaries have to be concentrated to the matrix between fractures. Also, the local minimum compressive principal stress can be significantly smaller than the minimum boundary stress, which influences the fractures extension. A comparison between the magnitudes of the local maximum (σ_I) and minimum (σ_{II}) compressive principal stresses over the fractured rock domain and the maximum compressive (σ_H) and minimum compressive (σ_h) stresses at the boundaries of the fractured rock domain was then made. Fig. 10, Fig. 11 shows the percentage of the area of the fractured rock domain where the local maximum compressive principal stress magnitude over the domain exceeds the boundary stresses magnitude and where the local minimum compressive principal stress is smaller than the minimum boundary stress magnitude.

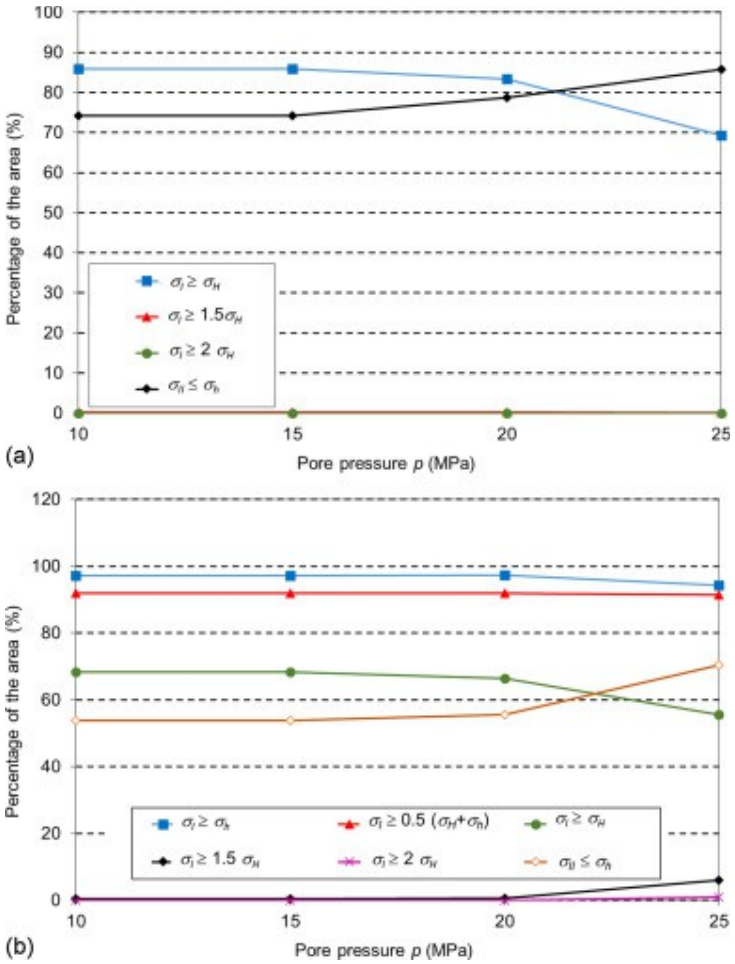

Download high-res image (365KB)

Download full-size image

Fig. 10. Comparison, in terms of the percentage of fractured rock domain area, of the magnitudes of the local maximum (σ_I) and minimum (σ_{II}) compressive principal stresses and the minimum (σ_h) and maximum (σ_H) boundary stresses magnitude, for different fluid pore pressure p levels for the (a) loading case SR1 (b) loading case SR2.

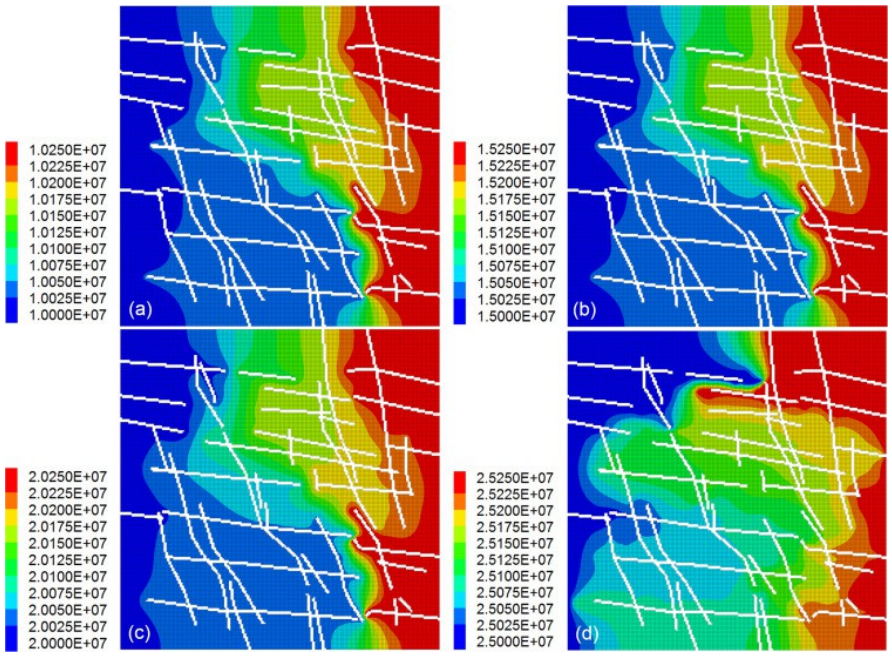

Download high-res image (4MB)

Download full-size image

Fig. 11. Contours of the fluid pore pressure [Pa] obtained for a fluid pore pressure *p* of (a) 10 MPa (b) 15 MPa (c) 20 MPa (d) 25 MPa (results obtained the loading case SR2).

From these figures it can be seen that in loading case SR1, the percentage of the fractured rock domain in which the local maximum compressive principal stress magnitude exceeds the boundary values ranges between approximately between 69% and 86% when the fluid pore pressures decreases from 25 MPa to 10 MPa, respectively. For all fluid pore pressure levels, the local maximum compressive principal stress magnitude is larger than 1.5 times the boundary stresses magnitude only in less than 0.3% of the fractured rock domain. The local maximum compressive principal stress magnitude does not exceed two times the boundary stresses magnitude at any point of the fractured rock domain. The percentage of the area of the fractured rock domain where the local minimum compressive principal stress magnitude is smaller than the minimum boundary stress magnitude ranges between 74% and 86% when the fluid pore pressure ranges between 10 and 25 MPa, respectively. For the loading case SR2, the percentage of the fractured rock domain where the maximum local compressive principal stress magnitude exceeds the minimum boundary stress magnitude ranges between approximately between 94% and 97% when the fluid pore pressures ranges between 25 MPa and 10 MPa, respectively. The percentage of the fractured rock domain where the local maximum compressive principal stress magnitude exceeds the maximum boundary stress magnitude ranges between approximately between 56% and 68% when the fluid pore pressures ranges between 25 MPa and 10 MPa, respectively. For a fluid pore pressure of 10 MPa, approximately 0.4% of the fractured rock domain has a stress value larger than 1.5 times the larger boundary stress (54 MPa) and in approximately 0.02% of the fractured rock domain, the stress is more than two times the maximum boundary stress magnitude. For a fluid pore pressure of 25 MPa, approximately 6% of the fractured rock domain has a local maximum compressive principal stress magnitude larger than 1.5 times the maximum boundary stress value, which is explained by an increase in the magnitude of this stress component at locations of some fracture tips and between close fractures. For a local maximum compressive principal stress magnitude larger than twice the maximum boundary stress value, this percentage is approximately 0.9%. These represent small areas of high maximum stress values or stress concentrations points in the fractured rock domain. The percentage of the fractured rock domain where the local minimum compressive principal stress magnitude is smaller than the minimum boundary stress magnitude ranges between approximately 54% and 70% of the fractured rock domain when the fluid pore pressure ranges between 10 and 25 MPa, respectively.

All these results indicate that at any point of interest over the fractured rock domain, any coupled hydro-mechanical behaviour is not dependent on boundary stresses, but on local stresses which can be very different from the boundary stress values over a significant region of the fractured rock domain.

4.3. Changes in fluid pore pressure field and flow paths

Tension failure regions lead to changes in fluid pore pressure distribution over the fractured rock domain and flow paths. To evaluate these changes, let us consider the loading case SR2, where the tension failure in the

intact rock is more prevalent. In this analysis, flow along the *x*-direction of the fractured rock domain is considered.

Fig. 11 shows the contour of the fluid pore pressure field obtained for a fluid pore pressure *p* of 10, 15, 20 and 25 MPa. Fig. 12 shows the contour of the fluid pore pressure gradient, obtained for a fluid pore pressure *p* of 10 and 25 MPa. In each grid element, the fluid pore pressure gradient is calculated by the square root of sum of squares of the gradients along the *x* and *y*-axis, considering the adjacent elements.

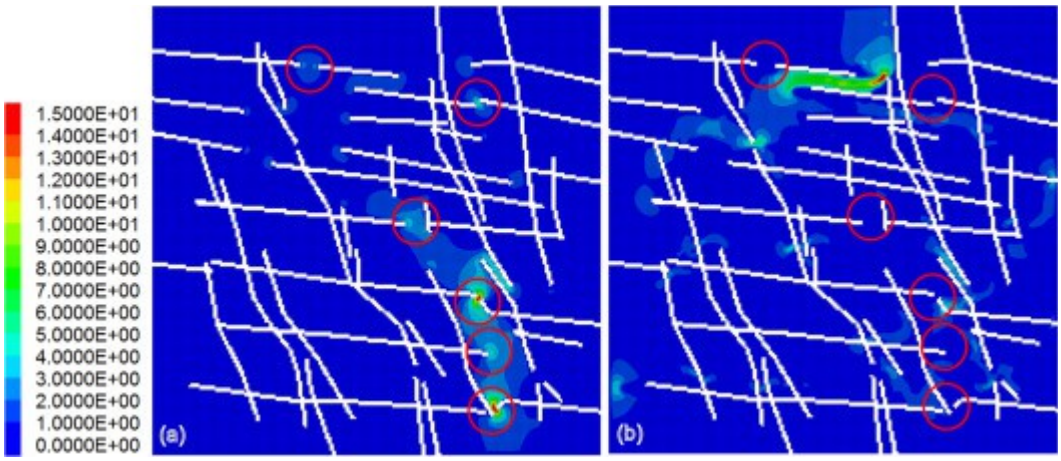

Download high-res image (1MB)

Download full-size image

Fig. 12. Contours of the fluid pore pressure gradient [MPa/m] for a fluid pore pressure *p* of (a) 10 MPa and (b) 25 MPa (results obtained for the loading case SR2).

Fig. 11 shows that for a fluid pore pressure *p* of 10, 15 and 20 MPa, the fluid pore pressure field is similar. But, when a pressure of 25 MPa is applied, the fluid pore pressure field changes, and there are regions of the fractured rock domain where the fluid pore pressure gradient decreases significantly. Fig. 12 shows that in six main zones, the fluid pore pressure gradient decreases significantly when the fluid pore pressure is increased from 10 to 25 MPa. This is explained by the fact that, with fluid pore pressure increased to 25 MPa, tension failure in the intact rock (see Fig. 6) generally increases significantly at the regions of high stress concentration (see Fig. 9) and new flow connections are created.

Fig. 13 shows the variation of the flow rate obtained at the points 1 to 5 (see Fig. 6) for a fluid pore pressure *p* of 10, 15, 20 and 25 MPa. By taking as a reference the flow rate curve obtained for a fluid pore pressure of 10 MPa, at the points number 1, 2 and 3, the flow rate is practically unchanged when a fluid pore pressure of 15 MPa is applied. Then, at the point number 1, the flow rate decreases by 0.7 times and increases by 1.3 times, when a fluid pore pressure of 20 and 25 is applied, respectively. In point number 2, the increases in flow rate are approximately 1.2 and 45 times when the fluid pore pressure increases to 20 and 25 MPa, respectively. In point number 3, the correspondent increases are approximately 1.1 and 650 times. In point 4, there is almost zero out-flow rate for a fluid pore pressure smaller than 25 MPa, which is justified by the very small permeability of the intact rock. But, for a fluid pore pressure of 25 MPa, significant changes in the flow paths occur due to tension failures in the intact rock, and hence, flow rate is observable at this point. In point

5, a very small flow rate is observed and only for a fluid pore pressure of 25 MPa. Because there is no new flow connection in this point, this is explained by the very small permeability of the intact rock.

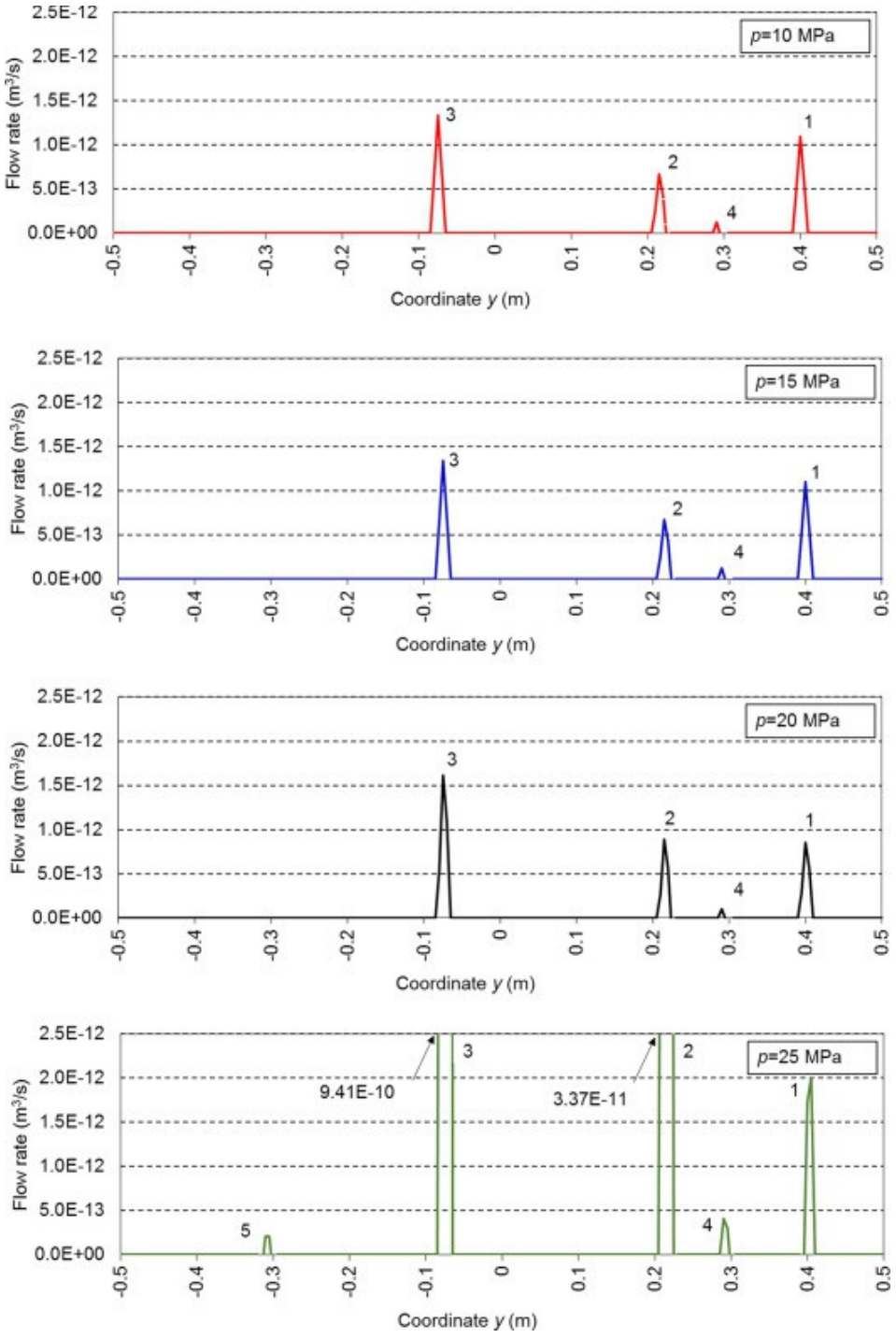

Download high-res image (610KB)

Download full-size image

Fig. 13. Variation of the out-flow rate along the left boundary of the fractured rock domain for a fluid pore pressure *p* of 10, 15, 20 and 25 MPa (results obtained for the loading case SR2).

4.4. Changes in permeability and flow anisotropy

In this section, changes in the equivalent permeability of the fractured rock domain and flow anisotropy are studied. Eqs. (8), (9)were used to calculate the equivalent permeability k_x and k_y, respectively of the fractured rock domain in the *x* and *y*-directions.

Fig. 14, Fig. 15 show the variation of the equivalent permeability k_x of the fractured rock domain as a function of fluid pore pressure, for the loading cases SR1 and SR2, respectively. The figures show the variation, as a function of fluid pore pressure *p*, of the equivalent permeability k_x, the percentage of the area of the fractured rock domain where tension failure in the intact rock occurs, and the average volumetric strains in the fractures and tension failure regions.

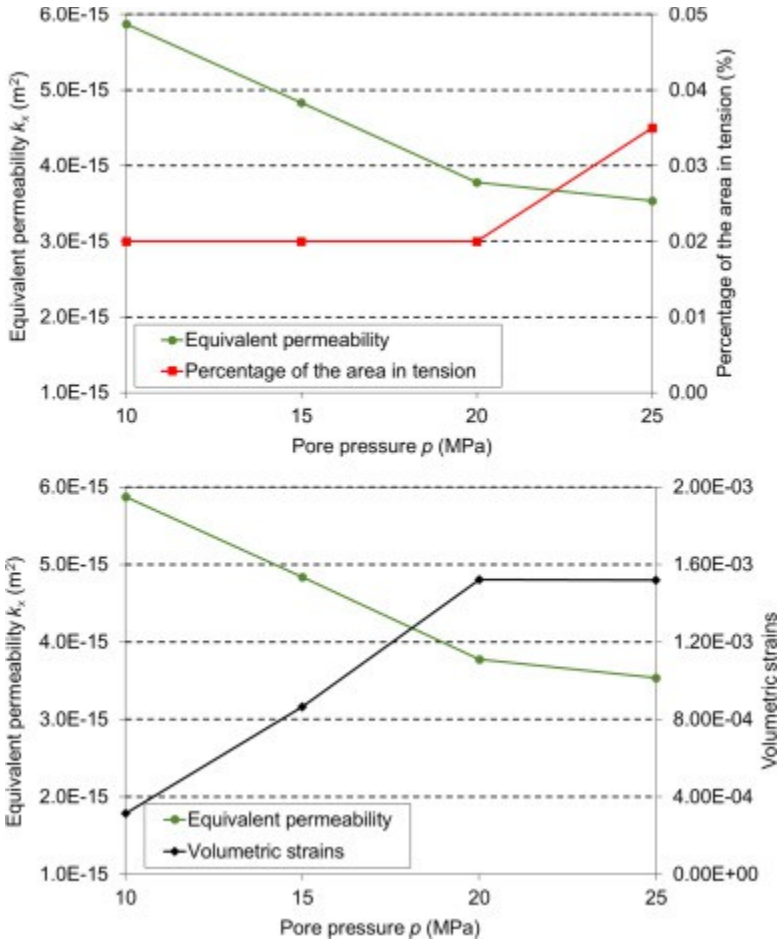

Download high-res image (343KB)

Download full-size image

Fig. 14. Variation of the equivalent permeability k_x, the percentage of the area of fracture rock domain in tension and the volumetric strains, as a function of pore pressure *p* (results obtained for the loading case SR1).

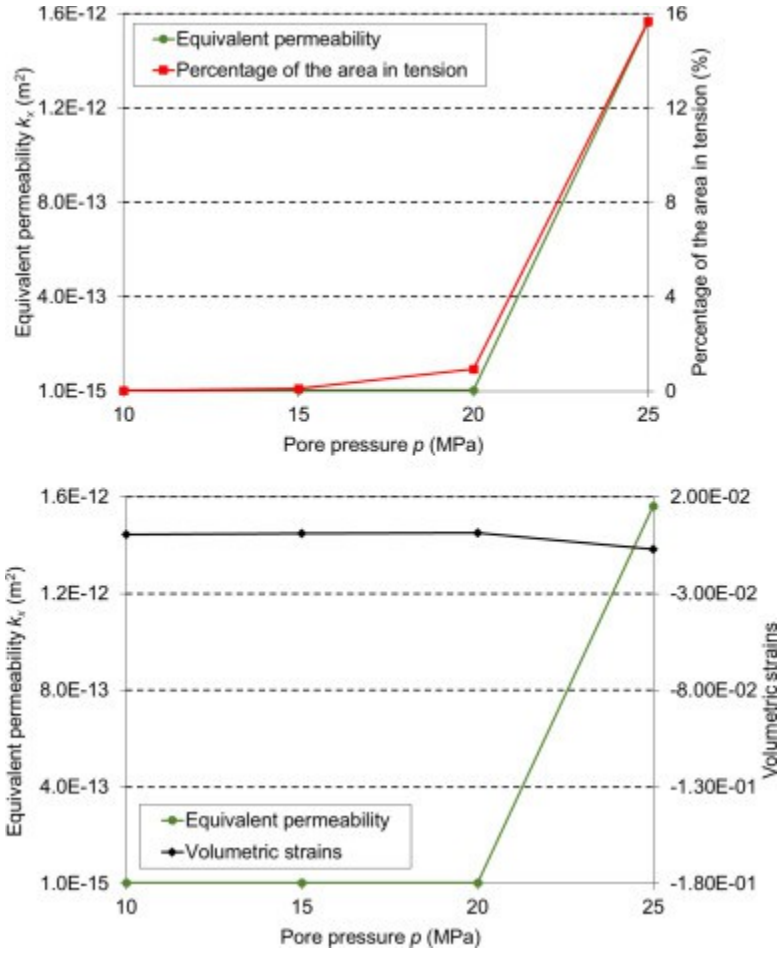

Download high-res image (306KB)

Download full-size image

Fig. 15. Variation of the equivalent permeability k_x, the percentage of the area of fracture rock domain in tension and the volumetric strains, as a function of pore pressure p (results obtained for the loading case SR2).

For loading case SR1, the permeability slightly decreases for a fluid pore pressure between 10 and 20 MPa, which is explained by the increase of the compressive volumetric strains (compression) in the fractures. When a 25 MPa fluid pore pressure is applied, the equivalent permeability still decreases although the area of the tension failure region increases. This is because the fractures sub-parallel to x-direction (fracture set 1), where the flow occurs, get more compressed (see Fig. 7) and no new flow connections are created by the tension failure regions in the intact rock to lead to an increase in the equivalent permeability.

For the loading case SR2, the equivalent permeability of the fractured rock domain slightly decreases when a fluid pore pressure of 15 MPa is applied, because the fractures get more compressed. Then, for a fluid pore pressure of 20 and 25 MPa, changes in permeability are mostly controlled by an increase of the tension regions. Changes in permeability are more significant for a fluid pore pressure of 25 MPa, which is approximately 90% of the minimum boundary stress magnitude, because of changes in the flow path caused by tension failure regions that connect the existing fractures (see Fig. 6). By taking as a reference the equivalent permeability obtained with a fluid pore pressure of 10 MPa, it is found that there is an increase in permeability of approximately 280 times when the fluid pore pressure is increased to 25 MPa.

Let us now analyse the results obtained for the flow anisotropy, which is obtained by taking the ratio between the permeability in the *x* and *y*-directions. The results are displayed in Fig. 16. In loading case SR1, the flow anisotropy is practically constant and equal to 1.2. This is because no significant tension failures occur in the intact rock. In loading case SR2, the flow anisotropy ranges between 1.3 and 1.6 for a fluid pore pressure ranging between 10 and 20 MPa. When the fluid pore pressure is 25 MPa, the increase in the permeability is much larger in the *x*-direction of the fractured rock domain, which is explained by the geometry of the fractured rock domain and a major increase of the flow in the *x*-direction when the tension failure regions connect the existing fractures. This leads to a significant increase in the flow anisotropy with is approximately 190.

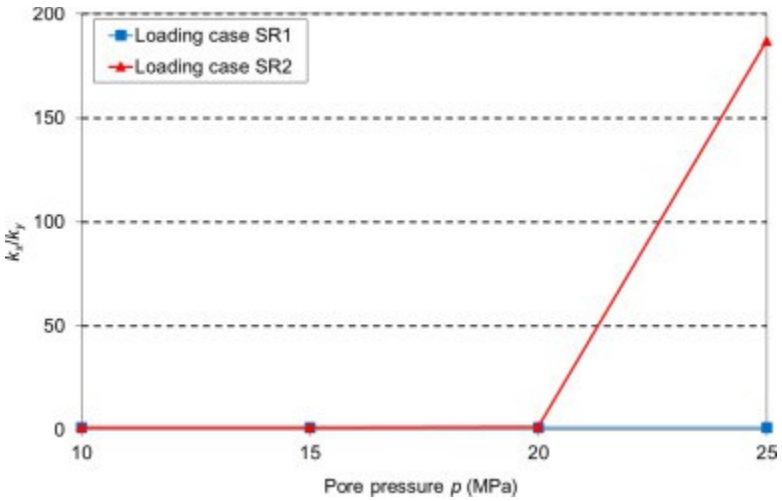

Download high-res image (139KB)

Download full-size image

Fig. 16. Flow anisotropy as a function of fluid pore pressure *p*.

5. Discussion

5.1. Effect of fluid pore pressure on the volumetric strains in the fracture elements

In Section 4, it was shown that for large fluid pore pressures, the fracture elements can get more compressed. To understand better this phenomenon, the model with one single fracture presented in Section 3.1 (see Fig. 3) was considered, with the exception that in this section, it is assumed that the fracture has stiffness or stress transfer through surface contacts. Three cases were considered: in case A, an elastic model, with the elastic properties indicated in Table 1, was considered for the fracture and intact rock; in case B, a Mohr–Coulomb model with the parameters listed in Table 1 was applied for the fracture and intact rock; in case C, the same Mohr–Coulomb model was applied for the fracture and intact rock, but by setting a very high cohesion in the fracture. By considering the loading case SR1, the mean values for the volumetric strains in the fracture were calculated for different levels of fluid pore pressure (Table 2). This table also shows the failure mechanism in the fracture. Results show that in case A, for higher levels of fluid pore pressure, the compressive volumetric strains increase and consequently the fracture aperture decreases. This is because the fluid pore pressure induces an expansion of the intact rock which swells into the softer fracture. It was found that the fracture aperture does not change if the fracture and intact rock have the same elastic properties. In case B, the fracture is more compressed until a fluid pore pressure of 25 MPa is applied. This is because for these pore

pressure levels, shear dilation and tension in the fracture are less significant than the compression induced by the expansion of the intact rock. For a 25 MPa fluid pore pressure, the two former effects are more significant than the latter effect and consequently, the fracture aperture increases. In case C, shear failure in the fracture is not observed because the cohesion is very high. However, tension failure occurs in the fracture for all fluid pore pressure levels. This results in an increase in the fracture aperture for higher levels of fluid pore pressure. This analysis concludes that the fractures aperture may decrease for large levels of constant fluid pore pressure, if tensile failure and shear dilation in the fracture are not enough to compensate for the compression induced by the intact rock into the softer fractures.

Table 2. Mean volumetric strains and failure mechanism in the fracture for different fluid pore pressure p levels.

Pore pressure p(MPa)	Case A		Case B		Case C	
	Strain	Failure	Strain	Failure	Strain	Failure
10	3.265E-09		5.135E-04	Shear	−8.264E-05	Tension
15	6.521E-09		1.063E-03	Shear	−2.933E-04	Tension
20	9.764E-09		1.532E-03	Shear tension	−5.631E-04	Tension
25	1.299E-08		2.432E-04	Shear tension	−2.197E-03	Tension

5.2. Effect of the tensile strength of the fractures

Results obtained in Section 4 were obtained by considering a null tensile strength σ_{tF} for fractures. Since the fractures are not modelled as empty aperture space, the fractures may have a non-zero tensile strength. A sensitivity study was made to analyse the influence of this parameter on the values of the equivalent permeability k_x of the fractured rock domain. By considering the loading case SR2, additional values of 1 and 5 MPa were considered for σ_{tF} and the results were compared with those obtained by considering a null value. Results of this comparison are shown in Table 3 for the different levels of fluid pore pressure. The table shows that the equivalent permeability does not vary with the tensile strength of the fractures. Tension failure was found to occur in the fractures only when the fluid pore pressure is 20 and 25 MPa. However, for all tensile strength values, the number of fracture elements where tension failure occurs and changes in volumetric strains are very similar. Consequently, differences in the equivalent permeability of the fractured rock domain obtained for the considered values of σ_{tF}, are practically negligible.

Table 3. Analysis of the influence of the tensile strength σ_{tF} of the fractures on the equivalent permeability k_x of the fractured rock domain (results obtained for the loading case SR2).

Pore pressure p(MPa)	Tensile strength σ_{tF}(MPa)	Equivalent permeability k_x(m²)
10	0	5.59E-15
	2	5.59E-15

Pore pressure p(MPa)	Tensile strength σ_{tF}(MPa)	Equivalent permeability k_x(m²)
	5	5.59E-15
	0	4.81E-15
15	**2**	4.81E-15
	5	4.81E-15
	0	5.08E-15
20	**2**	5.08E-15
	5	5.08E-15
	0	1.56E-12
25	**2**	1.56E-12
	5	1.60E-12

5.3. Effect of the fractures normal stiffness

This section presents the results of a sensitivity analysis to study the influence of the fractures normal stiffness k_n on the equivalent permeability k_x of the fractured rock domain. The fractures normal stiffness was set to 500 and 2000 GPa/m. Results obtained in this way were compared with those presented in Section 4, obtained with k_n equal to 1000 GPa/m. For the loading case SR2, results of this comparison are shown in Table 4. The table shows that the equivalent permeability of the fractured rock domain obtained with the three values for k_n is similar. Until a fluid pore pressure of 25 MPa is applied, the equivalent permeability of the fractured rock domain slightly increases as the fracture normal stiffness increases. For these fluid pore pressure levels, tension failure in the intact rock is not significant. Hence, when the fractures are stiffer, the fractures closure caused by the expansion of the intact rock, is smaller. This results in larger fractures aperture and consequently larger values of the equivalent permeability k_x, when larger fluid pore pressure values are considered. For a 25 MPa fluid pore pressure, changes in permeability are controlled by tension failure regions in the intact rock, which are more prevalent when the ratio between the stiffness of the elements of the intact rock and fractures is larger. This explains why, for this fluid pore pressure level, the equivalent permeability of the fractured rock domain increases by 4 times when the fracture normal stiffness decreases from 2000 GPa/m to 500 GPa/m.

Table 4. Analysis of the influence of the fractures normal stiffness k_n on the equivalent permeability k_x of the fractured rock domain (results obtained for the loading case SR2).

Pore pressure p(MPa)	Fracture normal stiffness k_n(GPa/m)	Equivalent permeability k_x (m²)
	500	4.94E-15
10	**1000**	5.59E-15
	2000	5.92E-15
15	500	3.60E-15
	1000	4.81E-15

Pore pressure p(MPa)	Fracture normal stiffness k_n(GPa/m)	Equivalent permeability k_x (m^2)
	2000	5.47E-15
	500	4.54E-15
20	**1000**	5.08E-15
	2000	5.87E-15
	500	3.98E-12
25	**1000**	1.56E-12
	2000	9.35E-13

5.4. Effect of the initial permeability of the tension failure regions

The assumption of the tension failure regions having the same initial permeability of the natural fractures may overestimate the equivalent permeability of the fractured rock domain, since not the whole damage area may form new fractures. A sensitivity analysis was done to study the influence of the permeability k_{TF} of the tension failure regions on the equivalent permeability k_x of the fractured rock domain. By considering the loading case SR2, k_{TF} was decreased by one and two orders of magnitude, to 4.5×10^{-14} and 4.5×10^{-15} m^2, respectively. The initial permeability of the natural fractures was kept equal to 4.5×10^{-13} m^3. A comparison of the results with those obtained in Section 4 is presented in Table 5 for different levels of fluid pore pressure. The table shows that for a fluid pore pressure of 10 and 15 MPa, in terms of absolute values, the equivalent permeability of the fractured rock domain decreases approximately 6% and 19% when the permeability of the tension failure regions decreases one and two orders of magnitude, respectively. For a 20MPa fluid pore pressure, the correspondent decreases are 13% and 27%. For a 25 MPa fluid pore pressure, the correspondent decreases are 18% and 28%. This concludes that for higher levels of fluid pore pressure, because the area of the tension failure regions is larger (see Fig.6), the influence of the permeability of the tension failure regions on the equivalent permeability of the fractured rock domain is more significant. However, in terms of relative terms, the variation of the equivalent permeability as a function of fluid pore pressure does not depend on the absolute value assigned to the permeability of the tension failure regions.

Table 5. Analysis of the influence of the permeability k_{TF} of the tension failure regions on the equivalent permeability k_x of the fractured rock domain (results obtained for the loading case SR2).

Pore pressure p(MPa)	Permeability k_{TF}(m^2)	Equivalent permeability k_x(m^2)
	4.5×10^{-13}	5.59E-15
10	**4.5×10^{-14}**	5.32E-15
	4.5×10^{-15}	4.61E-15
	4.5×10^{-13}	4.81E-15
15	**4.5×10^{-14}**	4.51E-15
	4.5×10^{-15}	3.85E-15
20	4.5×10^{-13}	5.08E-15

Pore pressure p(MPa)	Permeability k_{TF}(m²)	Equivalent permeability k_x(m²)
	4.5×10^{-14}	4.43E-15
	4.5×10^{-15}	3.72E-15
	4.5×10^{-13}	1.56E-12
25	**4.5×10^{-14}**	1.28E-12
	4.5×10^{-15}	1.13E-12

5.5. Effect of the power-law exponent

This section presents the results of a sensitivity analysis to study the influence of the power-law exponent n in Eq. (6) on the obtained results. By considering the loading case SR2, an additional exponent value of 10 was considered and the equivalent permeability k_x of the fractured rock domain was calculated for different levels of fluid pore pressure. The results were compared with those obtained with an exponent value of 3 and are shown in Table 6. Results show that permeability changes are much larger when a higher power-law exponent is considered, as to be expected. For a 25 MPa fluid pore pressure, the equivalent permeability k_x of the fractured rock domain obtained with an exponent of 10 is about seven orders of magnitude larger than the obtained with an exponent of 3. Other exponent values greater than 10 would lead to a very unrealistic magnitude of permeability changes. However, in spite of these increases in value for permeability changes, the same general conclusions as those reported in this paper, remain the same.

Table 6. Analysis of the influence of the power-law exponent n on the equivalent permeability k_x of the fractured rock domain (results obtained for the loading case SR2).

Pore pressure p(MPa)	Power law exponent n	Equivalent permeability k_x(m²)
10	3	5.59E-15
	10	3.63E-15
15	3	4.81E-15
	10	2.35E-15
20	3	5.08E-15
	10	6.02E-15
25	3	2.72E-13
	10	3.50E-06

6. Concluding Remarks

The focus of the study is on the hydro-mechanical behaviour of fractured rock masses for different levels of fluid pore pressure. An actual fracture pattern from outcrop mapping with complex geometry that includes two sets of fractures, fracture intersections, dead-end and curved fractures was used to study the influence of tension failure in the intact rock and fractures and shear displacement along the fractures on the equivalent permeability of a realistic fractured rock domain. The conclusions from the obtained results may be summarised as follows:

In an isotropic loading case, failure regions were found to be insignificant. When the ratio of maximum to minimum boundary stresses is equal to 2, for fluid pore pressure values approaching the magnitude of the minimum boundary stress, tension failure occurs in the intact rock. However, it does not result in simple fracture extensions; instead, it results in failure regions with irregular shapes in the neighbourhood of fracture endings or between fractures of each other in close vicinity. Their development depends on the values of the ratio between the two boundary stresses, the local minimum principal stress, the fluid pore pressure, the tensile strength of the intact rock and the geometry of the fractured rock domain.

The occurrence of pore-pressure induced tension failure regions leads to significant changes in the distributions of principal stresses over the fractured rock domain. For a large fluid pore pressure value, the minimum value for the minimum principal stress over the fractured rock domain was found to be approximately 55% of the minimum boundary stress magnitude. In terms of area, the minimum principal stress over the fractured rock domain was found to be smaller than the minimum boundary stress magnitude in approximately 75% of the fractured rock domain area. The local maximum compressive principal stress was found to be larger than the boundary maximum compressive principal stress magnitude in approximately 50% of the fractured rock domain area. Because the permeability of fractured rock masses is sensitivity to the stress concentration areas, a careful hydro-mechanical analysis should be carried out which includes the effect of all dead-end fractures and not to neglect them as is commonly the practise in fracture hydrogeology.

The volumetric strains in the fracture elements can be more compressive for large fluid pore pressure values if the tensile strains and shear dilation in the fractures are not enough to compensate for fracture closure caused by an expansion of the rock matrix that swells into the softer fractures.

Significant changes in flow paths and equivalent permeability of the fractured rock domain are in general to be expected when the ratio of maximum to minimum boundary stresses is equal to 2 and the fluid pore pressure is approximately 90% of the minimum boundary stress magnitude. The equivalent permeability of the fractured rock domain is about two orders of magnitude greater than its initial value. In such a scenario, the fluid pore pressure field over the fractured rock domain becomes smoother and the pressure gradients over the domain are generally smaller, because new flow connections have been created. This decrease in the fluid pore pressure gradient is associated with an increase in the ratio between the magnitudes of the local maximum and minimum compressive principal stresses. This may have implications on studies of solute transport in fractured rocks under hydro-mechanical processes.

The magnitude of permeability changes may depend on some model parameters such as the fractures normal stiffness, the permeability of the tension failure regions and the power-law exponent of the law used to relate changes in permeability to changes in porosity. These have been studied in a sensitivity analysis. However, the general conclusions reported on this paper do not depend on the absolute values of these parameters.

The conclusions from the present study bring out some interesting aspects of fracture rock hydromechanics that deserve further studies and that need to be accounted for in modelling hydro-mechanical behaviour of fractured rocks. As further work it is proposed, firstly, to consider other fractured rock domains with different

density, orientation and length for the fracture sets, and secondly, to generalise the numerical approach presented in this paper to study the coupled hydro-mechanical effects in 3D fractured rock domains.

Acknowledgements

The authors gratefully acknowledge the comments of the two reviewers, including those of Ki-Bok Min. We also would like to thank the Swedish Geological Survey (SGU), grant number 1724, for providing financial support to research reported in this paper. Additional support was provided by the U.S. Department of Energy under contract No. DE-AC02-05CH11231.

References

1. J. Rutqvist, O. Stephansson **The role of hydro-mechanical coupling in fractured rock engineering**
   Hydrogeol J, 11 (2003), pp. 7-40
2. C.F. Tsang, A. Niemi **Deep hydrogeology: a discussion of issues and research needs**
   Hydrogeol J, 21 (2013), pp. 1687-1690
3. K.B. Min, J. Rutqvist, C.F. Tsang, L. Jing **Stress-dependent permeability of fractured rock masses: a numerical study**
   Int J Rock Mech Min Sci, 41 (2004), pp. 1191-1210
4. B. Amadei, O. Stephansson **Rock Stress and its Measurements**
   Chapman & Hall, London (1997)
5. C. Ljunggren, Y. Chang, T. Janson, R. Christiansson **An overview of rock stress measurement methods**
   Int J Rock Mech Min Sci, 40 (2003), pp. 975-989
6. Baghbanan, L. Jing **Stress effects on permeability in a fractured rock mass with correlated fracture length and aperture**
   Int J Rock Mech Min Sci, 45 (2008), pp. 1320-1334
7. P.S. Lang, A. Paluszny, R.W. Zimmerman **Permeability tensor of three-dimensional fractured porous rock and a comparison to trace map predictions**
   J Geophys Res Solid Earth, 119 (2014), pp. 6288-6307
8. Q. Lei, J.P. Latham, J. Xiang, C.F. Tsang, P. Lang, L. Guo **Effects of geomechanical changes on the validity of a discrete fracture network representation of a realistic two-dimensional fractured rock**
   Int J Rock Mech Min Sci, 70 (2014), pp. 507-523
9. D.J. Sanderson, X. Zhang **Critical stress localization of flow associated with deformation of well-fractured rock masses, with implications for mineral deposits**
   Geol Soc Lond Spec Publ, 155 (1999), pp. 69-81
10. X. Zhang, D.J. Sanderson **Effects of stress on the two-dimensional permeability tensor of natural fracture networks**
    Geophys J Int, 125 (1996), pp. 912-924
11. X. Zhang, D.J. Sanderson, A.J. Barker **Numerical study of fluid flow of deforming fractured rocks using dual permeability model**
    Geophys J Int, 151 (2002), pp. 452-468
12. M. Nejati, A. Paluszny, R. Zimmerman **A disk-shaped domain integral method for the computation of stress intensity factors using tethahedral meshes**
    Int J Sol Struct, 69 (2015), pp. 230-251
13. A. Paluszny, R. Zimmerman **Numerical simulation of multiple 3D fracture propagation using arbitrary meshes**
    Comput Methods Appl Mech Eng, 200 (2011), pp. 953-966

14. A. Paluszny, X.H. Tang, R.W. Zimmerman **Fracture and impulse based finite-discrete element modeling of fragmentation**
Comput Mech, 52 (2013), pp. 1071-1084
15. Ghassemi A, Kelkar S, McClure M. Geothermal Code Comparison Study: Problems 2, 3 and 6. *In: Proceedings of the 4th Workshop on Geothermal Reservoir Engineering*. Stanford; 2015.
16. J. Rutqvist, C. Leung, A. Hoch, Y. Wang, Z. Wang **Linked multicontinuum and crack tensor approach for modeling of coupled geomechanics, fluid flow and transport in fractured rock**
J Rock Mech Geotech Eng, 5 (2013), pp. 18-31
17. Itasca. FLAC3D, Version 5.0. User's Manual. Itasca Consulting Group, Minneapolis; 2012.
18. J.P. Latham, J. Xiang, M. Belayneh, H.M. Nick, C.F. Tsang, M. Blunt **Modelling stress-dependent permeability in fractured rock including effects of propagation and bending fractures**
Int J Rock Mech Min Sci, 57 (2013), pp. 100-112
19. P.B. Attewell, I.W. Farmer **Principles of Engineering Geology**
Wiley, New York (1976)
20. Zhao J. Properties of rock materials. In: *Rock Mechanics For Civil Engineering*, 49 p. www.epf.ch/en/ensei/Rock-Mechanics/ENS-080312-EN-Notes-Chapter-4.pdf.
21. D.D. Pollard, P. Segall **Theoretical displacements and stresses near fractures in rock: with applications to faults, joints, veins, dikes, and solution surfaces**
B.K. Atkinson (Ed.), Fracture Mechanics of Rock, Academic Press Inc, United States (1987), pp. 277-349
22. F. Cappa, J. Rutqvist **Modeling of coupled deformation and permeability evolution during fault reactivation induced by deep underground injection of CO_2**
Int J Greenhouse Gas Control, 5 (2011), pp. 336-346
23. L.Y. Chin, R. Raghavan, L.K. Thomas **Fully coupled geomechanics and fluid flow analysis of wells with stress-dependent permeability**
Soc Petrol Eng J, 5 (2000), pp. 32-45
24. Rinaldi, J. Rutqvist, F. Cappa **Geomechanical effects of CO_2 leakage through fault zones during large-scale underground injection**
Int J Greenhouse Gas Control, 20 (2014), pp. 117-131
25. P.A. Witherspoon, J.S.Y. Wang, K. Iwai, J.E. Gale **Validity of cubic law for fluid flow in a deformable rock fracture**
Water Resour Res, 16 (1980), pp. 1016-1024
26. P. Renard, G. de Marsily **Calculating equivalent permeability: a review**
Adv Water Resour, 20 (1997), pp. 253-278
27. J. Rutqvist, A. Bäckström, M. Chijimatsu, *et al*. **A multiple-code simulation study of the long-term EDZ evolution of geological nuclear waste repositories**
Environ Geol, 57 (2009), pp. 1313-1324